

Shear wave arrivals in surface microseismic data

Ben Witten, Summer Montgomery, and Brad Artman, Spectraseis

Three-component acquisition of fracture monitoring data using broadband receivers captures event energy “missing” in 1-C surface microseismic surveys

Summary

There is a common misconception in microseismic monitoring that shear arrivals are more difficult to detect at the surface than compressional arrivals. This is despite the fact that, for common fracture types, the energy released in the form of shear waves is greater than compressional energy. To reconcile such claims, it has been assumed that the near surface has higher attenuation for S-waves than P-waves. In this paper we demonstrate through modeling and field data acquired in 2011 and 2012, that S-waves are not only detectable at the surface, but in our experience have larger amplitudes than P-waves. To unequivocally observe this phenomenon the full wavefield must be sampled with 3-component instruments for microseismic data acquisition.

We conclude that:

1) field results support our theoretical and numerical predictions of the larger S-wave content in wavefields generated by common fracture mechanisms,

2) the frequency content of the constituent components scales roughly with velocity, and

3) the S-wave attenuation would have to be unrealistically different than the P-wave attenuation to make the S-arrival undetectable when a P-arrival is recorded. Lastly, given a sufficiently accurate velocity model, the S-waves can be used to accurately locate microseismic events, including events that are undetectable using P-waves alone.

S-waves are not only detectable at the surface, but in our experience have larger amplitudes than P-waves.

Introduction

The ability to record shear waves from microseismic events at the surface has been dismissed in the literature (Eisner et al., 2010a; Duncan and Eisner, 2010). However, the data on which this conclusion has been based is largely single component, vertical geophones with a 15 Hz corner frequency. When three component (3C) broadband receivers with a flat frequency response between 0.1 and 1000 Hz are used to acquire the data, shear arrivals are seen. Kolinsky et al.



(2009) show shear arrivals in the 3C data set they analyzed; they state that S-waves are weak due to attenuation and occur at lower frequencies. Since frequency scales proportional to velocity, the latter observation is to be expected. Figure 1 is a field example where the S-wave has higher amplitudes than the P-wave. (This figure will be discussed further in the field data section below.)

This observation is more often the rule than the exception, as should be expected for common fracture mechanisms. We will demonstrate, with elastic modeling and 3C field data, that large quantities of S-wave energy from microseismic fractures can be recorded at the surface, and can be used to locate and characterize fracture events.

Modeling

For common fracture mechanisms, the energy released in the form of S-waves is much greater than that in the form of P-waves. Various studies have inverted for source type from microseismic data. Eisner et al. (2010b) show a strong fit to a double-couple (DC) mechanism for their data. However, Baig and Urbancic (2010) determine that the events they studied have a larger compensated linear vector dipole (CLVD) component.

Theoretically, fractures must be some combination of DC, CLVD, and isotropic components. Since dominantly isotropic sources are unlikely to be induced, we analyze only the DC and CLVD mechanisms.

Aki and Richards (2002) derive the ratio of S/P energy released for a DC event is equal to

$$\frac{\Omega^s}{\Omega^p} = 2 \left(\frac{v_p}{v_s} \right)^3, \quad (1)$$

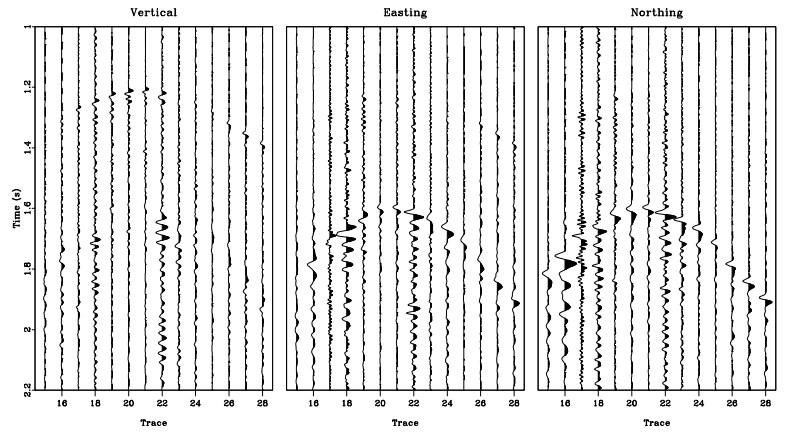


Figure 1: In-line gather for a microseismic event from 3C sensors spanning 3575 m. The three panels are the vertical, easting, and northing components. The S-wave arrivals have much higher amplitudes on the horizontal components than the P-wave arrival on the vertical.

where Ω^s and Ω^p are the S- and P-wave energy over the unit sphere, and v_p/v_s is the ratio of the P-wave to the S-wave velocity at the source location. For realistic v_p/v_s values between 1.6 and 2.2 at event depth, the S/P energy ratio varies from 8.2 to 21. Therefore, a DC event generates around an order of magnitude more S-wave energy than P-wave energy.

For common fracture mechanisms, the energy released in the form of S-waves is much greater than that in the form of P-waves.

The CLVD mechanism has a smaller S/P energy ratio than a DC mechanism. For this failure type, the energy ratio over the unit sphere (Lokmer and Bean, 2010) is

$$\frac{\Omega^s}{\Omega^p} = \frac{3}{2} \left(\frac{v_p}{v_s} \right)^3. \quad (2)$$

Considering the same range of velocity ratios as above, we expect the S/P energy ratio for a CLVD fracture in realistic rocks to vary from 6.1 to 16.

We now numerically model both DC and CLVD events to investigate the relative energy of the P and S arrivals on a surface acquisition plane. The non-zero components of the stress tensor for the DC source are $S_{xy} = S_{yx} = 1$, and for the CLVD source $S_{xx} = S_{zz} = 1$ and $S_{yy} = -2$. In both scenarios, the source is located at 2200 m depth and located in the center of a 7600 m x 7600 m surface array. The velocity is

a 1-D function that changes nonlinearly with depth. We use a constant v_p/v_s of 1.7, $Q_p = Q_s = 100$, and account for geometric spreading.

Figure 2 shows RMS amplitude on the vertical component recorded at the surface for the S (left) and P (right) arrivals for a DC source mechanism (top row) and a CLVD source (bottom row). Each row has been scaled together to the maximum energy. In the DC results, there is more S-wave than P-wave energy at the near offsets (ignoring the nodes) and slightly less at far offsets. For the CLVD source, there is more P-wave energy at near offsets, but more S-wave energy at far offsets.

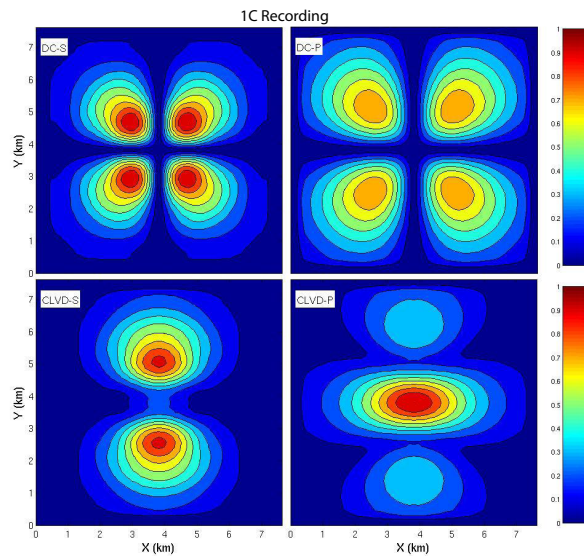


Figure 2: S (left) and P (right) relative RMS amplitudes at the surface in the vertical direction for a DC (top) and CLVD (bottom) source mechanism. Each source type is scaled to the maximum in the row.

To attenuate the S arrivals \leq the P in the DC model, as suggested in Duncan and Eisner (2010), the average Q_s over the entire travel path must be ≤ 75 when $Q_p = 100$.

Field results support our theoretical and numerical predictions of the larger S-wave content in wavefields generated by common fracture mechanisms.

In contrast, Figure 3 shows the RMS amplitude at the surface, similar to Figure 2, using all three components for both source mechanisms and wave types. The S/P RMS amplitude ratio increases considerably at all surface locations compared to the single component modeling above. The maximum of the S-wave in Figure 3 is 6.3 times greater than the maximum of the P-wave for the DC source, and 3.7 times larger for the CLVD source. To reduce the maximum of the S-wave such

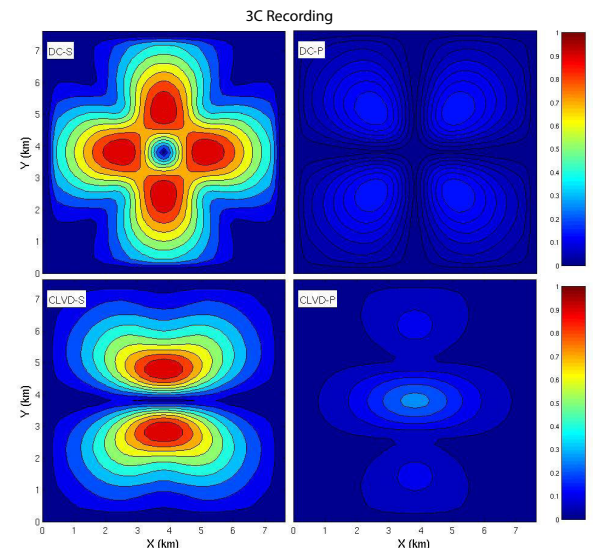


Figure 3: S (left) and P (right) relative RMS amplitude at the surface using three components for a DC (top) and CLVD (bottom) source mechanism. Each source type is scaled to the maximum in the row.

that it is equal to the maximum of the P-wave for the CLVD source with $Q_p = 100$, Q_s would have to be 20. For a DC source this discrepancy is even greater, requiring a Q_s of 9 along the entire travel path.

Field Data

Of the half dozen 3C data sets that we are familiar with at the time of writing, all of them contain significant S-wave energy. These data sets, which include multiple plays in North America, usually have S-wave arrivals with higher amplitudes than the P-wave arrivals. We present two recent examples here.

Texas, USA

The first field data example comes from an October 2011 survey in Texas where the treatment well is approximately 2000 m deep. The array was a 14 x 10 grid of 3C broadband sensors spaced 275 m apart. As previously noted, Figure 1 shows both P and S arrivals clearly. This is taken from an in-line

(perpendicular to the horizontal well) gather for all three components bandpass filtered between 1 and 100Hz, and plotted on the same amplitude scale. The P-wave is most clearly visible on the vertical component, although the S-wave is also identifiable and of comparable amplitude on this component. On the two horizontal components, the S-wave has larger amplitudes than the P-wave does on the vertical component.

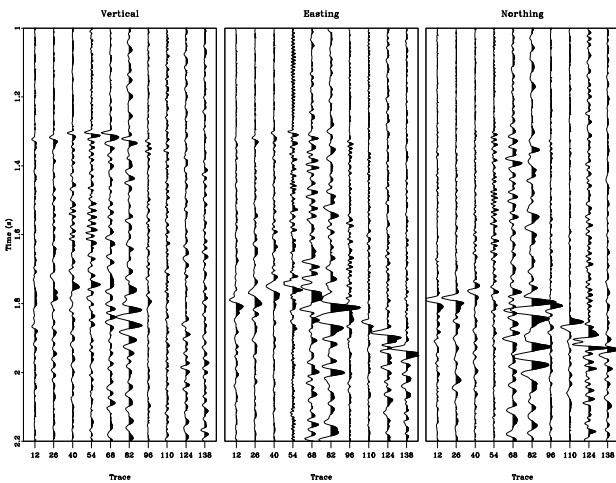


Figure 4: Cross-line gather for a microseismic event from 3C sensors spanning 2475 m. The three panels are the vertical, easting, and northing components.

Figure 4 is the cross-line gather for the same event at the same amplitude scale as in Figure 1. Figures 1 and 4 intersect at trace 26. By inspecting these figures together we can see an observable radiation pattern for the event. On the northing component of Figure 4 there is a polarity reversal across the array, while for the easting component there is no polarity reversal. The opposite is true in Figure 1. These observations indicate a DC source type.

Figure 5 is a spectrogram for trace 20 in Figure 1. All three panels use the same color scale. The frequency axis goes from 1 to 100 Hz. The P-wave arrival, strongest in the left panel, has energy between 10 and 70 Hz with a maximum around 60 Hz. The S-wave arrival, delayed 0.6 s, contains energy between 2 and 40 Hz, with a maximum at 18 Hz.

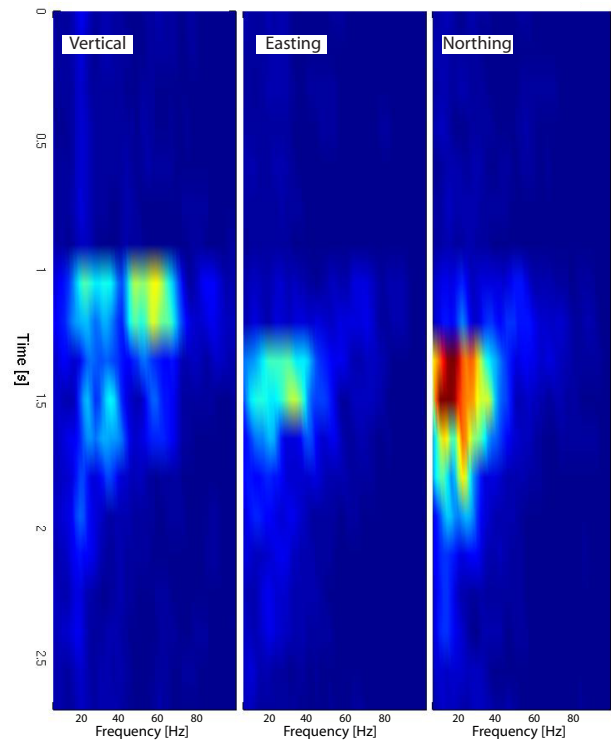


Figure 5: Spectrogram for trace 20 in Figure 1.

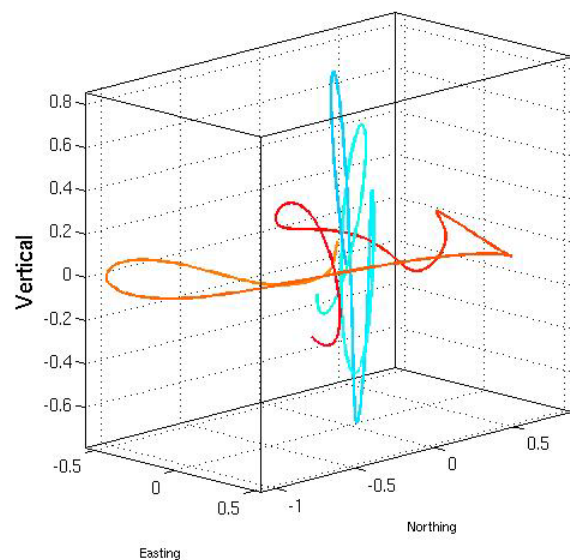
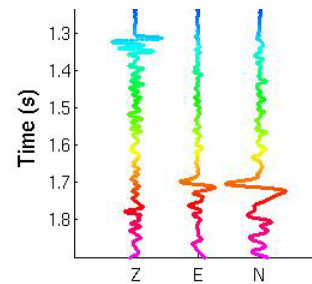


Figure 6: Trace 20 from Figure 1 for the vertical, easting, and northing components and the particle motion hodogram colored by time.

Again we note that since frequency scales with velocity, we expect the lower frequency content of the S mode, which needs fewer wavelengths to travel from source depth to the array. This low frequency energy would not have been recorded without the broadband sensors deployed for this survey.

Figure 6 shows two representations of trace 20 from Figure 1 color coded by time for the vertical, easting, and northing components. As the hodogram highlights, the P-wave is vertically polarized while the S-wave is horizontally polarized.

In this data set, every event detected had larger amplitude S- wave arrivals than P-wave arrivals at the surface. In fact, most events have no detectable P-wave arrival. The S-wave

The S-wave arrivals provided the most valuable information for locating microseismic events.

arrivals provided the most valuable information for locating the microseismic events. An S-wave velocity model was generated from well-log data in the area and a wave-equation imaging technique was applied to locate events using the S-wave data. Figure 7 shows a depth slice at the well depth through a signal-to-noise (S/N) volume generated by time-reverse imaging (Witten and Artman, 2011) for the data shown in Figures 1 and 4. There is a clear focus of energy with a high S/N ratio of 6 near the treatment location for this stage.

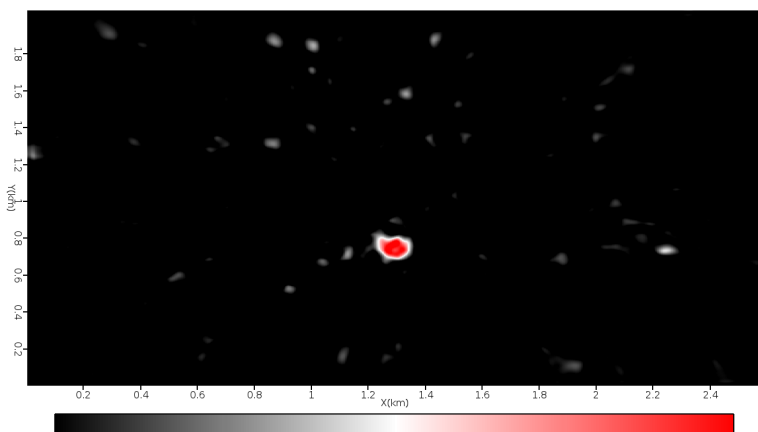


Figure 7: Signal-to-noise time-reverse image using the data shown in Figures 1 and 4.

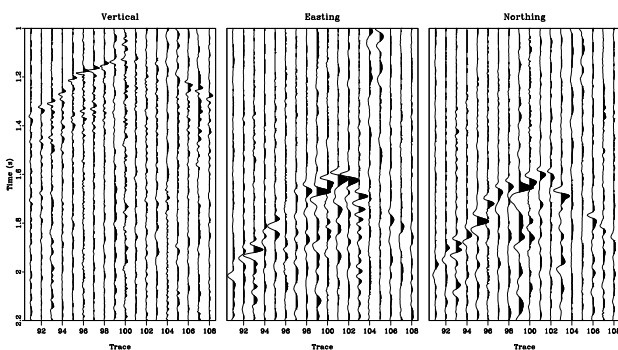


Figure 8: In-line data for the vertical, easting, and northing components for the BC data spanning 3825 m. and 4.

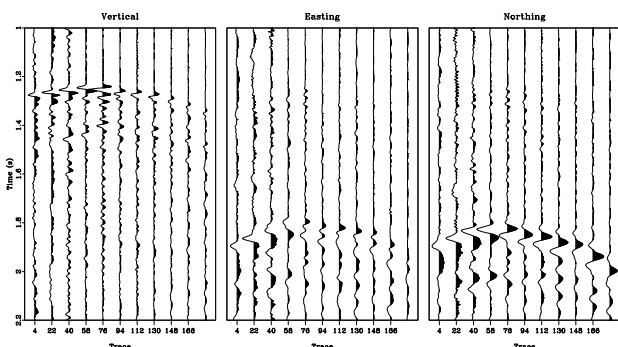


Figure 9: Cross-line data for the vertical, easting, and northing components for the BC data set spanning 2250 m. and 4.

British Columbia, Canada

Our second example of S-wave data recorded at the surface comes from British Columbia, Canada. The data were acquired in February 2012 with 3C broadband sensors in an 11 x 18 grid with 250 m spacing. There were two nearly parallel wells at approximately 2100 m depth that were stimulated. Figures 8 and 9 show an in-line and cross-line gather for the vertical, easting and northing components for an event. The traces intersect at trace number 94. This event is representative of the many thousands in this data set containing strong P and S arrivals.

There is a clear polarity reversal seen in the cross-line data. At the time of writing, work is ongoing



with this data to locate and characterize the source mechanisms of the microseismic events. The S-wave arrivals are proving beneficial to focus the events more strongly than when using the P-wave arrivals alone.

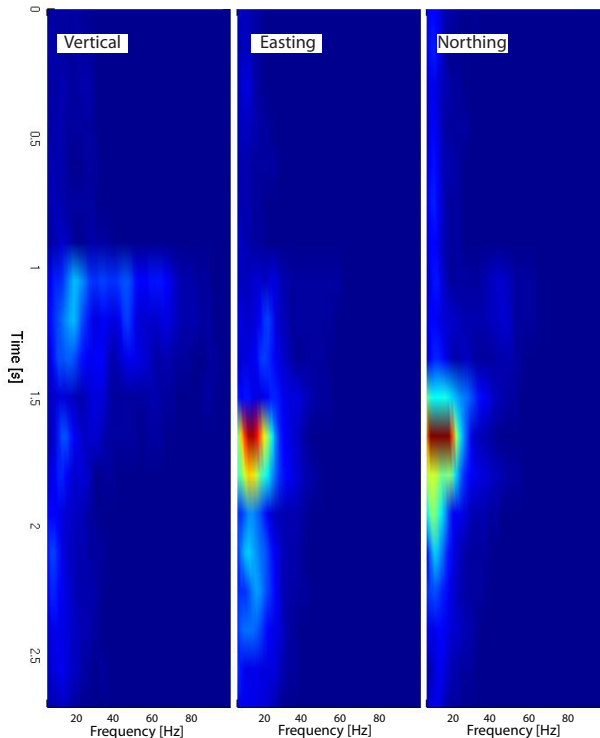


Figure 10: Spectrogram for trace 95 in Figure 8.

Figure 10 shows a spectrogram for trace 95 in the previous figures. The majority of the energy for both the P- and S-wave arrivals exists between 2 and 20 Hz with energy extending up to 70 Hz for the P-wave arrival. The energy captured on each of the horizontal components is more than 2 times greater than the energy captured on the vertical component.

Conclusions

In contrast to earlier studies, we have shown that S-wave emissions from microseismic fracture events are detected at the surface with appropriate equipment and survey design. Furthermore, not only can S-waves be detected, they are often the largest arrivals in the microseismic records. Full wavefield sampling using three-component sensors demonstrates this unequivocally.

Data from recent microseismic surveys show that our modeling assumptions are validated in the field, where we see significant amounts of S-wave energy at lower frequencies in surface recording arrays. Broadband sensors are very useful because they record, with fidelity, the low frequency bandwidth of these arrivals.

S-wave energy can be used to confidently locate and characterize fracture events, even when higher frequency P-wave energy is weak or undetectable.

Given a suitable S-wave velocity model, the S-wave energy can then be used to confidently locate and characterize fracture events in (x,y,z)-space, even when higher frequency P-wave energy is weak or undetectable.

Acknowledgements

We would like to thank Forest Oil and Progress Energy for allowing publication of their data.

Aki, K., and P. Richards, 2002, Quantitative seismology: University Science Books.

Baig, A., and T. Urbancic, 2010, Microseismic moment tensors: A path to understand frac growth: The Leading Edge, 29, 320–324.

Duncan, P., and L. Eisner, 2010, Reservoir characterization using surface microseismic monitoring: Geophysics, 75, A139–A146.

Eisner, L., B. J. Husley, P. Duncan, D. Jurick, H. Werner, and W. Keller, 2010a, Comparison of surface and borehole locations of induced seismicity: Geophysical Prospecting, 58, 809–820.

Eisner, L., S. Williams-Stroud, A. Hill, P. Duncan, and M. Thornton, 2010b, Beyond the dots in the box: microseismicity-constrained fracture models for reservoir simulation: The Leading Edge, 29, 326–333.

Kolinsky, P., L. Eisner, V. Grechka, D. Jurick, and P. Duncan, 2009, Observation of shear-wave splitting from microseismicity induced by hydraulic fracturing: A non-vti story: 71st Conference and Exhibition, Extended abstracts, EAGE, X014.

Lokmer, I., and C. Bean, 2010, Properties of the near-field term and its effect on polarisation analysis and source locations of long-period (lp) and very-long-period (vlp) seismic events at volcanoes: Journal of Volcanology and Geothermal Research, 192, 35–47.

Witten, B., and B. Artman, 2011, Signal-to-noise estimates of time-reverse images: Geophysics, 76, MA1–MA10.

Ben Witten is a Senior Geophysicist for Spectraseis in Denver, CO. He graduated with a BS in Applied Mathematics from Columbia University and then received a MS in Geophysics from Stanford University. Mr. Witten's work focusses primarily on modeling and imaging of passive seismic data. In particular, he is active in the research and development of Time-reverse imaging (TRI) and applying TRI to customer microseismic monitoring data to deliver high quality imaging and characterization of induced fracture networks.



Summer Montgomery has over 12 years of geophysics experience, including petrophysical research, marine seismic data acquisition and processing, and borehole data acquisition and interpretation. Ms. Montgomery has a BS in Geophysical Engineering from the Colorado School of Mines. She is a Geophysicist for Spectraseis in Denver, CO, where she specializes in processing and imaging microseismic monitoring data.



For enquiries please call +1 888 791 7244 or email:

USA

salesusa@spectraseis.com

www.spectraseis.com

Canada

salescanada@spectraseis.com